

FrontierNet: Learning Visual Cues to Explore

Boyang Sun¹, Hanzhi Chen², Stefan Leutenegger², Cesar Cadena¹, Marc Pollefeys^{1,3}, Hermann Blum^{1,4}

Abstract—Exploration of unknown environments is crucial for autonomous robots; it allows them to actively reason and decide on what new data to acquire for tasks such as mapping, object discovery, and environmental assessment. Existing methods, such as frontier-based methods, rely heavily on 3D map operations, which are limited by map quality and often overlook valuable context from visual cues. This work aims at leveraging 2D visual cues for efficient autonomous exploration, addressing the limitations of extracting goal poses from a 3D map. We propose an image-only frontier-based exploration system, with FrontierNet as a core component developed in this work. FrontierNet is a learning-based model that (i) detects frontiers, and (ii) predicts their information gain, from posed RGB images enhanced by monocular depth priors. Our approach provides an alternative to existing 3D-dependent exploration systems, achieving a 16% improvement in early-stage exploration efficiency, as validated through extensive simulations and real-world experiments. Source code will be released publicly.

Index Terms—Perception and Autonomy, Motion and Path Planning, Deep Learning

I. INTRODUCTION

AUTONOMOUS exploration requires a robot to navigate through an unknown environment to accomplish tasks such as building a digital map, locating objects, or, more broadly, gathering environmental information. This capability is critical for a wide range of applications, including infrastructure modeling and inspection [1], [2], search and rescue [3], [4], crop monitoring [5], [6], and object search [7].

The key to efficient autonomous exploration—whether maximizing mapping volume, acquiring semantic knowledge, or improving reconstruction quality—is identifying optimal poses for the robot to reach. Existing methods, often based on the 3D map constructed by the robot, either focus on extracting the map boundary [8] or iteratively sample poses or paths within the map and select the most suitable ones [9]. These approaches differ in perspective: one derives poses from the 3D map by calculating optimal poses directly, the other samples poses and evaluates them against the map to find the optimal ones. Thus, both approaches leverage the 3D map information to guide exploration. At the same time, they are also inherently limited by the quality of the 3D map, which depends on factors like sensor accuracy, reconstruction methods, and map representation. For instance, artifacts in the 3D map can lead to false, unreachable goal poses, emphasizing the need for precise 3D geometry. Furthermore, these 3D-based methods often overlook valuable appearance information from RGB images, resulting in redundant and inefficient exploration paths.

In contrast to **dense** 3D map operations typically used in exploration, the final solution to it often results in **sparse** outputs, such as a set of candidate poses. Sparse representations like these have proven effective and efficient for various

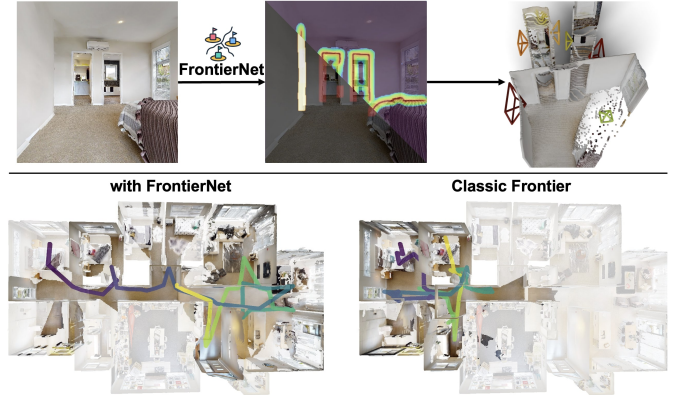


Fig. 1: **Top**: FrontierNet processes a RGB image (left) to detect frontier pixels and their information gain (middle), registering candidate viewpoints with varying priorities in 3D (right). **Bottom**: Using FrontierNet, our exploration system prioritizes visiting unknown regions with greater potential of unmapped volume, achieving higher efficiency.

robotic tasks, including exploration and navigation [10]–[18]. We argue that achieving similarly sparse outputs does not inherently require dense 3D operation. For instance, a human can readily identify key spots to move to uncover unknown spaces from a single RGB image. These spots, which represent the explicit boundary of the current viewpoint, are akin to 3D frontiers but can be inferred without relying on a 3D map. This inference relies solely on cues from RGB images, while effectively extracting both geometric and appearance information. Additionally, one can estimate how much unknown space each spot might reveal, informed by contextual image details—a level of inference that is challenging and costly in 3D. Fig. 2 provides an abstract comparison of identifying candidate poses for exploration using visual cues versus dense 3D geometric information.

Building on these observations, this work explores how to extract explicit boundary indicators from RGB images for autonomous exploration. We propose an image-only frontier-based system for efficient exploration, introducing **FrontierNet**, a learning-based model for hybrid frontier detection and information gain prediction. This model directly predicts frontiers and their information gain from individual RGB frames, linking exploration decisions in 3D space with visual cues. Our system supports posed RGB input and leverages 3D cues from monocular depth priors.

The contributions of this paper are summarized as follows:

- An efficient autonomous exploration system, which works with individual posed RGB images as the input.
- A learning-based frontier and information gain predictor integrated in the proposed system.
- Extensive simulation experiments and real-world tests that validate the proposed system.

¹ETH Zurich, ²Technical University of Munich, ³ Microsoft, ⁴ Uni Bonn

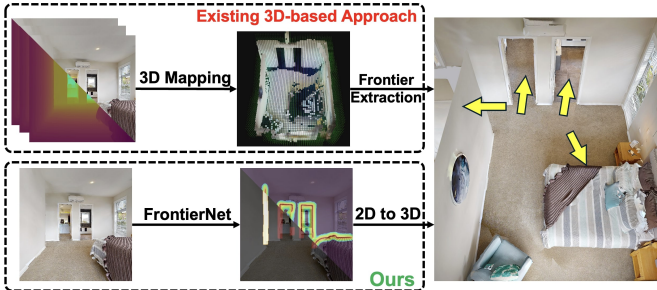


Fig. 2: FrontierNet learns to extract regions for exploration from visual cues in RGB images. Unlike existing methods, it avoids operations on dense 3D maps at the detection stage, which are sensitive to map quality, and often miss crucial appearance information.

II. RELATED WORK

In this section, we investigate works for autonomous exploration. Various approaches have been proposed. As introduced in Section I, two major types: *frontier-based* and *sampling-based* methods are commonly used to solve the problem. Most of these methods rely on a 3D representation of the world and operate on top of it, they have different focus and model the environment differently. Early works use conventional 3D representations, such as occupancy grid [8], [19], [20], signed distance field [11], [21] and 3D point cloud [17], with which frontier-based methods iterate through the map and extract the map boundary, while sampling-based methods evaluate sampled viewpoints using different metrics, such as map entropy and uncertainty [11], [12]. More recent work has tried to use learning-based computer vision algorithms to help design evaluation metrics. In [15], a 3D occupancy prediction model is used to estimate the information gain of each frontier. [22] uses similar scene completion network for viewpoint evaluation. With the emerging new 3D representations, recent works have proposed the use of neural implicit representation [23], [24], or 3D Gaussian [25]–[27].

The aforementioned works have shown that 3D geometry representation can be helpful for exploration; recent approaches build on this by incorporating appearance information into the 3D representation for improved performance. One line of work introduces object-level semantics into the maps, [13], [15], [28] introduce semantic information into trajectory and viewpoint evaluation, and [29] uses semantic-informed loop closure for better localization accuracy during exploration. Another branch of work model exploration as a decision-making problem, they use reinforcement learning to solve the problem that often includes the color image as input [16], [30]. More recent works try to utilize the power of vision foundation models and large language models for interactive, human-like exploration [10], [31], [32].

The mentioned works have shown that appearance is a valuable resource for exploration. Although appearance information has been utilized, it is either tightly integrated with volumetric maps for metric design or serves as input for independent vision algorithms. However, we observe that appearance cues can be directly leveraged during detection to identify boundaries without relying on 3D representations. These cues also allow for the evaluation of boundaries, eliminating the need to integrate them into intermediate visual task models.

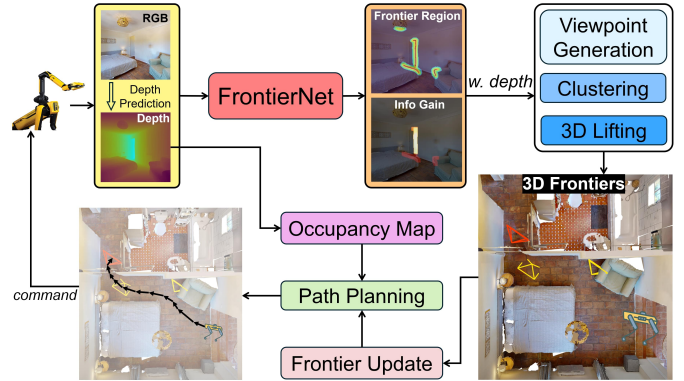


Fig. 3: **System Overview:** Our system processes posed RGB images with a depth prediction model [33] to generate estimated depth. FrontierNet uses RGB-D input to predict 2D frontier regions and their info gain, which are transformed into sparse 3D frontiers with different gains (colored frustums). These frontiers are tracked, and the planning module selects the next best goal and plans a path using the occupancy map.

III. METHOD

A. Problem Statement

The goal of this work is to let a camera-equipped robot autonomously explore an environment. The robot moves, collects images, and uses them to maximize knowledge of the environment. To quantify this knowledge, we follow prior works [11], [14], [15] and choose mapped volume as the metric. A static environment can be modeled as a bounded volume $\mathbf{V} \subset \mathbb{R}^3$, each point $\mathbf{v} \in \mathbf{V}$ is associated with occupancy probability $P(\mathbf{v})$. Initially, all the points have occupancy probability $P(\mathbf{v}) = 0.5$, indicating occupancy as *unknown*. The occupancy probability of each point gets updated when the robot extends its map covering it. It becomes a *known* point, i.e., $\mathbf{v} \in \mathbf{V}_{\text{known}}$, where $\mathbf{V}_{\text{known}} \subset \mathbf{V}$. We aim at finding a sequence of poses $\mathbf{x} = (\mathbf{p}, \mathbf{q})$, $\mathbf{p} \in \mathbb{R}^3$ and $\mathbf{q} \in so(3)$, which the robot follows and collects images to maximize $|\mathbf{V}_{\text{known}}|$.

B. System Overview

An overview diagram of the proposed system can be seen in Fig. 3. The core component is our FrontierNet, which performs joint frontier detection and information gain prediction, followed by 3D-anchoring and planning steps. During exploration, our system maintains a frontier updating mechanism that tracks changes across all frontiers. The path planning module selects the next goal frontier and plans a path.

C. Learning to Detect Frontiers from Visual Appearance

We adapt the frontier definition from [8], which describes a frontier as a known-free 3D voxel adjacent to unknown space. Commonly, frontiers are therefore detected from 3D voxel maps. Instead, we consider *frontier pixels* as the 2D projection of 3D frontier voxels within a camera’s observed space and want to learn a detection model that identifies these frontier pixels directly in an image.

Additionally, classical frontier definitions treat all frontiers equally, ignoring variations in their potential to observe additional space. Recent works [12], [15], [22] address this by defining metrics—commonly referred to as information gain—to differentiate the importance of frontiers. In this work, we define the additional observable volume previously

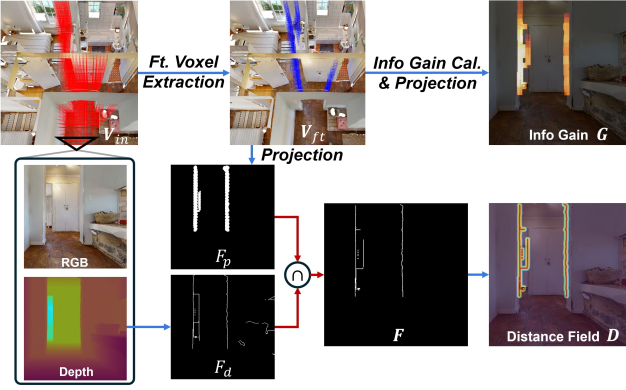


Fig. 4: **Ground Truth Generation:** For a sampled camera pose in the voxelized scene, 3D frontier voxels are calculated and projected onto the camera frame using ground truth 3D occupancy grid. Merging the projection with the depth discontinuity mask produces a refined and less noisy frontier pixels mask \mathbf{F} , which is used to calculate the distance field map \mathbf{D} . Additionally, projecting the info gain of each frontier voxel onto the camera frame generates the info gain map \mathbf{G} .

unknown from a frontier as its *info gain* and train our model to also predict it from the input image. This prediction only depends individual input image, assuming no prior exploration. To unify frontier pixels detection with info gain prediction, we employ a two-head UNet-like structure, **FrontierNet**, and frame the task as an image-to-image prediction. It utilizes both the color image and its corresponding monocular depth prior as input and jointly predicts the frontier pixels and info gain.

For the frontier pixels detection head, inspired by recent advances in line detection [34], [35], our approach models the frontier pixels using a distance field \mathbf{D} . Given an input RGB-D image $\mathbf{I} \in \mathbb{R}^{H \times W \times 4}$, FrontierNet $f_{\text{FtNet}}(\cdot)$ predicts a distance field $\mathbf{D} \in \mathbb{R}^{H \times W}$, where the value of each pixel (i, j) in \mathbf{D} is the distance on the image plane to the closest pixel within the frontier pixel. Specifically,

$$\tilde{\mathbf{D}} = f_{\text{FtNet}}(\mathbf{I}), \quad (1)$$

$$\mathbf{D}[i, j] = \min_{(x, y) \in \mathcal{F}} \|(i, j) - (x, y)\|_2, \quad (2)$$

where $\tilde{\mathbf{D}}$ is the prediction, \mathcal{F} denotes pixel set corresponding to the frontier pixels in \mathbf{I} , and $\|\cdot\|_2$ is the Euclidean distance.

For the info gain prediction head, following our definition, the projected 3D voxels with their calculated info gain form a 2D info gain value map $\mathbf{G} \in \mathbb{R}^{H \times W}$. The calculation of \mathbf{G} will be discussed in III-D. Regressing the pixel-wise value with high variance can be challenging and sensitive to noisy input [36], we reformulate info gain prediction as a multi-class classification problem. We discretize the value spectrum of the info gain into K bins and train the model to predict the bin index. Given the input RGB-D image \mathbf{I} , our model predicts the multi-class info gain map $\mathbf{Y} \in \mathbb{N}^{H \times W}$ as:

$$\tilde{\mathbf{Y}} = f_{\text{FtNet}}(\mathbf{I}), \quad (3)$$

$$\mathbf{Y}[i, j] = \text{bin}(\mathbf{G}[i, j], K), \quad (4)$$

where $\tilde{\mathbf{Y}}$ is the prediction, $\mathbf{G}[i, j]$ is the info gain at pixel (i, j) , and $\text{bin}(\cdot, K)$ maps $\mathbf{G}[i, j]$ into one of K discrete classes.

D. Data Generation and Model Training

Few works have attempted to learn the detection of the frontier or the estimation of information gain from images. Some

studies leverage intermediate vision models to estimate information in unknown space, such as map completion approaches [15], [22], which take a 3D map as input and hallucinate unknown areas, then a information gain can be computed. We use 3D information to generate ground truth data and directly supervise our model $f_{\text{FtNet}}(\cdot)$ without intermediate steps. Specifically, we generate ground truth data from the Habitat-Matterport 3D (HM3D) [37], a dataset of real-world textured 3D scans.

Fig. 4 illustrates the ground truth generation pipeline. We voxelize the entire 3D scene and sample camera viewpoints within the voxelized space. The voxel grid is categorized into two classes: voxels inside the camera view (\mathbf{V}_{in}) and those outside (\mathbf{V}_{out}). Following the logic of classic 3D frontier detection, frontier voxels (\mathbf{V}_{ft}) are identified within \mathbf{V}_{in} as those adjacent to \mathbf{V}_{out} . \mathbf{V}_{ft} are projected onto the image plane to generate a binary prior \mathbf{F}_p , representing the initial frontier pixel. Since frontier pixels are typically associated with gaps in appearance and geometry, which often correspond to depth discontinuities, we create a binary depth discontinuity mask \mathbf{F}_d by thresholding the depth gradient map. The refined frontier pixels mask \mathbf{F} is obtained by intersecting \mathbf{F}_p and \mathbf{F}_d , i.e., $\mathbf{F} = \mathbf{F}_p \cap \mathbf{F}_d$. Finally, we generate the ground truth distance field \mathbf{D} from \mathbf{F} .

To obtain the ground truth info gain, we calculate the additional observable volume for each frontier voxel \mathbf{v} from \mathbf{V}_{ft} and propagate this value to pixels in the frontier pixel. Ideally, this would involve checking each \mathbf{v} in \mathbf{V}_{ft} and identifying the viewpoint that maximizes observable volume in \mathbf{V}_{out} ; however, this operation is computationally intractable. We approximate this by sub-sampling 10% of \mathbf{V}_{ft} . For each sampled voxel, we determine an optimal viewpoint by calculating the 3D direction from \mathbf{V}_{in} to \mathbf{V}_{out} at its 3D position. We then linearly interpolate the estimated info gain values of the remaining frontier voxels in \mathbf{V}_{ft} . This approximation is reasonable because (i) at any frontier voxel, the optimal viewing direction to observe unknown space is generally toward regions outside the observed area, and (ii) frontier voxels that are spatially close are also close to the same unknown regions, therefore providing similar info gain. We generate both \mathbf{F}_p and \mathbf{G} by performing per-pixel ray-casting. For each ray, we compute its distance to all voxels from \mathbf{V}_{ft} and retain only those within a specified range r , effectively controlling the extent of the info gain map. The info gain value of the pixel is assigned as the maximum info gain from all voxels close enough to the ray.

We train both heads of FrontierNet simultaneously. One head regresses the distance field \mathbf{D} , while the other classifies the multi-class info gain mask \mathbf{Y} . The input RGB-D image is processed by a shared encoder-decoder structure based on a ResNet [38] backbone pretrained on ImageNet [39]. The shared output is then passed to two separate heads, each consisting of three 2D convolution layers.

To supervise the distance field \mathbf{D} , we apply a normalization process similar to [34]: $\hat{\mathbf{D}} = -\log(\mathbf{D}/r)$ For the info gain classification head, we discretize the info gain values into 11 ($K = 11$ in Eq. 4) classes.

The total loss is the weighted sum of the two heads:

$$\mathcal{L} = \alpha \cdot \mathcal{L}(\tilde{\mathbf{D}}, \hat{\mathbf{D}}) + \mathcal{L}_Y(\tilde{\mathbf{Y}}, \mathbf{Y}), \quad (5)$$



Fig. 5: **3D Frontiers Generation:** Each frontier pixel is assigned a 2D viewing angle derived from the depth gradient. Combined with the info gain, 2D clustering is applied to obtain sparse 2D frontier clusters with associated viewing directions (middle). The foreground and background depths near the frontier pixels are then utilized to lift each clustered 2D frontier into 3D space.

where \mathcal{L}_D is the L1 loss on the normalized distance field, \mathcal{L}_Y is the combined cross entropy and multi-class Dice loss on the multi-class map, and α is a hyper-parameter.

E. Anchoring Frontier in 3D

We design a post-processing stage that extracts sparse candidate frontiers with viewing directions from the output of FrontierNet and anchors them in 3D as targets for the robot to approach. As an initial step, it recovers the frontier pixels and info gain value map (\mathbf{F}, \mathbf{G}) from the FrontierNet outputs (\mathbf{D}, \mathbf{Y}), as defined by Eqs. 1 and 3:

$$\mathbf{F}[x, y] = \begin{cases} 1 & \text{if } \mathbf{D}[x, y] < l \\ 0 & \text{otherwise} \end{cases}, \quad (6)$$

$$\mathbf{G}[i, j] = \text{bin}^{-1}(\mathbf{Y}[i, j], K), \quad (7)$$

where l is the inclusion parameter for \mathbf{F} , and $\text{bin}^{-1}(\cdot, K)$ reverses the binning in 4 to the lower bound of the bin.

Fig. 5 illustrates the process of transforming (\mathbf{F}, \mathbf{G}) into sparse candidate viewpoints within the 3D scene for exploration. It consists of three main steps: viewpoint generation, clustering, and 3D lifting.

1) *Viewpoint Generation:* Viewpoint selection is often achieved through 3D sampling-based approaches [11]–[13], [26], [40]. Our viewpoint generation method leverages monocular depth priors, eliminating the need for sampling operations in 3D. For each frontier pixel (x, y) , namely $\mathbf{F}[x, y] = 1$, we determine a 2D viewing direction from the depth gradient in its neighborhood. The gradient points along the steepest depth increase in the local window, typically from the foreground to the background. The inverse of this gradient points toward the occluded space behind the foreground, providing the viewing direction $\phi_{(x,y)}$ for (x, y) .

2) *Clustering:* 3D frontier-based methods typically perform clustering on frontier voxels after detection [12], [14], [15]. Similarly, we cluster 2D frontier pixels. We construct a feature vector $\mathbf{Ft}[x, y] = [x, y, \phi_{(x,y)}, g_{(x,y)}]$ for each frontier pixel. Here, $\phi_{(x,y)}$ is the viewing angle introduced above, and $g_{(x,y)} = \mathbf{G}[x, y]$ is the info gain at (x, y) . By performing HDBSCAN [41] with these per-pixel features, we obtain sparse 2D frontier clusters, denoted \mathbf{Ft}_i^{2D} , for $i = 1, 2, \dots, k$. For each cluster, its feature $[\bar{x}_i, \bar{y}_i, \bar{\phi}_i, \bar{g}_i]$ is calculated as:

- The cluster coordinate (\bar{x}_i, \bar{y}_i) is the centroid pixel of its member pixels, ensuring it lies within the frontier pixels.
- The cluster’s viewing direction $\bar{\phi}_i$ is the weighted average of the viewing directions of its member pixels, with weights assigned based on each pixel’s info gain.

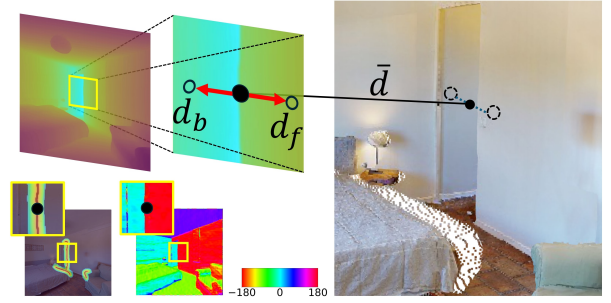


Fig. 6: **Viewpoint Generation and 3D Lifting:** Our method computes a gradient map (bottom right) from the depth map. For each frontier pixel, foreground and background depths are sampled along the positive and negative gradient directions. The negative gradient also defines the 2D viewing angle, while the average of the two depths is used for lifting the pixel to 3D.

- The cluster’s info gain \bar{g}_i is the average of all member pixels.

3) *2D to 3D Lifting:* To position the 2D frontiers in 3D, we assign each frontier pixel (x, y) a depth that lifts it to an intermediate location between the foreground and the background of the frontier. The lifting process begins with the same gradient map derived from the depth image as in viewpoint generation III-E1. Two depth values, d_b and d_f , are sampled along the positive and negative directions of the local depth gradient to approximate the depth of the background and foreground, respectively. The depth of the frontier is then calculated as the average, $\bar{d} = (d_b + d_f)/2$. Fig. 6 provides an example of this lifting operation for a single pixel. Although using the depth prediction in the process may not provide the exact metric depth everywhere, this approximation reliably captures the free space between the foreground and background, ensuring robustness against depth inaccuracies. To further enhance robustness, the depth values are assigned before clustering, and the final depth of each clustered frontier is taken as the average depth of its member pixels. Once the depth value for \mathbf{Ft}_i^{2D} is determined, its 3D viewpoint is obtained by lifting $\bar{\phi}_i$ using the same depth value.

The entire anchoring process outputs a set of sparse 3D frontiers: $\mathbf{Ft}_i^{3D} = [\bar{\mathbf{p}}_i, \bar{\mathbf{q}}_i, \bar{g}_i]$ for $i = 1, 2, \dots, k$, where $\bar{\mathbf{p}}_i$ and $\bar{\mathbf{q}}_i$ represent the 3D position and orientation of the frontier, and \bar{g}_i denotes its info gain.

F. Exploration Planning

1) *Frontier Update:* Our system incorporates three primary update mechanisms for managing 3D frontiers, which operate concurrently as the robot explores.

New Frontier Integration: As new frontiers are detected and lifted to 3D, they are either added to the current frontier list as new entries or merged with existing ones. Merging occurs because the same frontiers can be registered multiple times in 3D when viewed from different images capturing the same region. Following a similar metric used in the literature for 3D clustering, each new frontier’s 3D position and viewing direction are compared to those of all existing frontiers. If both the distance of the positions and the angle between the orientations of the new frontier and an existing frontier are below a threshold, the two are merged, with the properties of the merged frontier computed as the average of the two. Otherwise, the new frontier is registered independently. Since the 3D frontiers are sparse, this merging process remains computationally efficient, even as the list expands.

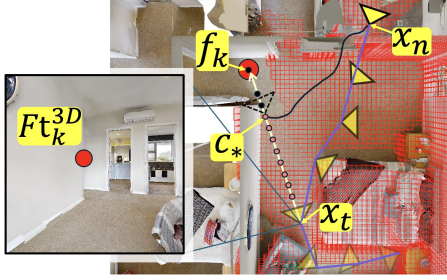


Fig. 7: **Path Planning:** When the robot is at pose \mathbf{x}_t , the next goal frontier \mathbf{f}_k , detected at a previous pose \mathbf{x}_r , lies outside the current 3D occupancy map. Our planner samples along the edge $(\mathbf{f}_k, \mathbf{x}_r)$ to find the point \mathbf{c}_* within the map that is closest to \mathbf{f}_k . The robot then plans a 3D path to \mathbf{c}_* and incrementally maps and moves toward \mathbf{f}_k , using the edge as a directional prior.

Info Gain Adjustment: Though our system extracts frontiers without relying on a 3D map, we can optionally maintain a 3D occupancy map to support frontier updates and path planning, as both steps require an awareness of the 3D environment. Specifically, the initial info gain, \bar{g}_i , of a frontier \mathbf{Ft}_i^{3D} reflects the unknown volume it can potentially observe without any information of the explored region. As the robot progresses the exploration, \bar{g}_i is expected to decrease. To capture this reduction, we project the known voxels \mathbf{v} from $\mathbf{V}_{\text{known}}$ from the current occupancy map into the image frame at $[\bar{\mathbf{p}}_i, \bar{\mathbf{q}}_i]$, and filter out projections that lie outside the image frame or are too distant, creating the set $\mathbf{V}_{\text{known}}^i$. The updated info gain for \mathbf{Ft}_i^{3D} is then computed as: $\bar{g}_i^* = \bar{g}_i - |\mathbf{V}_{\text{known}}^i|$.

Invalid Frontier Removal: A frontier \mathbf{Ft}_i^{3D} is considered invalid based on two criteria: a) if its updated info gain \bar{g}_i^* falls below a minimum threshold g^{\min} , or b) if its viewpoint is similar to previously visited poses. This implies that the additional region indicated by a frontier has already been explored, or the frontier itself has been visited. To enforce the second criterion, we compare the Euclidean distance of positions and relative angle between $\bar{\mathbf{p}}_i, \bar{\mathbf{q}}_i$ and the downsampled robot trajectory. This second criterion is especially important when the info gain \bar{g}_i is inaccurately high in ambiguous scenarios, preventing some frontiers from being cleared effectively.

2) *Path Planning:* Our path planning approach leverages frontier utility u to guide the robot’s exploration. Similar to [11], the utility of a candidate frontier \mathbf{Ft}_i^{3D} is defined as its info gain divided by the distance required to reach it:

$$u(\mathbf{x}_r, \mathbf{Ft}_i^{3D}) = \frac{\bar{g}_i^*}{\|\bar{\mathbf{p}}_r - \bar{\mathbf{p}}_i\|}, \quad (8)$$

where $\mathbf{x}_r = [\bar{\mathbf{p}}_r, \bar{\mathbf{q}}_r]$ is the current pose of the robot. The frontier with the highest utility is then selected as the next goal frontier. This results in a natural balance between exploring nearby areas and pursuing more distant frontiers that may reveal larger unknown regions without needing additional tuning parameters.

During exploration, our planner maintains a rooted tree structure $T = (\mathcal{N}, \mathcal{E})$ that includes two types of nodes, $\mathcal{N} = \{\mathbf{x}_0, \mathbf{x}_1, \mathbf{x}_2, \dots, \mathbf{x}_n, \mathbf{f}_1, \mathbf{f}_2, \dots, \mathbf{f}_m\}$, where $\mathbf{x}_{(\cdot)}$ represents robot poses, and $\mathbf{f}_{(\cdot)}$ denotes poses of valid frontiers. The nodes $\mathbf{x}_{(\cdot)}$ form the main branch of the tree as a single chain: $\mathbf{x}_0 \rightarrow \mathbf{x}_1 \rightarrow \mathbf{x}_2 \rightarrow \dots \rightarrow \mathbf{x}_n$. If the robot detects a frontier \mathbf{f}_j at a pose \mathbf{x}_i , then \mathbf{f}_j is assigned \mathbf{x}_i as its parent, creating an edge $(\mathbf{x}_i, \mathbf{f}_j) \in \mathcal{E}$. Fig. 7 illustrates a planning example of our system using the tree structure. This frontier-parent linkage is

a key feature enabled by FrontierNet, which detects frontiers at the boundary between known and unknown regions, ensuring they are always within the camera’s field of view and visible. This guarantees that at least one ray connects the camera’s optical center to each clustered frontier. Consequently, the edge between the parent robot pose, and its frontier children represent both visibility and feasible traversal from the robot’s pose to the frontier. When the next goal frontier \mathbf{f}_k lies beyond the current 3D map, our planner samples 3D points $\mathbf{c}_{(\cdot)}$ along the edge to its parent robot pose $\mathbf{x}_i = \text{parent}(\mathbf{f}_k)$, verifying whether each sampled point $\mathbf{c}_{(\cdot)}$ exists within the current occupancy map. Upon identifying the first valid point \mathbf{c}_* within the map, it is able to perform 3D path planning to reach \mathbf{c}_* . To ultimately reach \mathbf{f}_k , the robot uses the direct line between \mathbf{c}_* and \mathbf{f}_k as a prior and performs 3D path planning along this route while it maps more regions ahead.

Our planning approach is especially useful and reliable when the goal frontier lies far outside the current occupancy map or when inaccuracies arise due to scale differences in monocular depth estimation. Furthermore, it supports path planning in extreme scenarios, such as when computational or storage resources are limited or when depth sensing or prediction is highly unreliable, by enabling exploration without relying on the occupancy map at all.

IV. EXPERIMENT AND RESULT

A. Experiments Setup

Our exploration system is tested on scenes from the validation set of HM3D, which are not seen during the training phase of FrontierNet and the chosen monocular depth model. We simulate camera viewpoints and render images with Open3D [42]. RGB images are rendered at a resolution of 480×480 . For depth data, we use two options: (1) rendered ground-truth depth at the same resolution, and (2) predicted depth generated with Metric3D v2 [33]. We employ a Python wrapper of Octomap [43] to build the occupancy map. Our low-level 3D path planner is implemented using the Open Motion Planning Library (OMPL) [44].

For quantitative evaluation, camera motion is simulated by interpolating the planned path into dense, discrete poses and teleporting the camera through these poses. We benchmark our method against a classic frontier method [8], and more recent approaches NBVP [11], and SEER [15]. No open-source code is available for [8], so we implement it ourselves. We use the ROS implementations for [11] and [15] to get the exploration paths. Autonomous exploration lacks a standardized test setup, and existing methods are generally tested on a limited number of scenarios. Specifically, the two baselines selected for the benchmarking are evaluated in two scenes. To assess the efficiency and generalizability of our method, we expand the test scenarios to 10 diverse scenes, varying in layout, size, appearance, and number of floors. For each scene, we initialize the camera at several different starting locations and allow it to explore until there are no remaining frontiers, or it reaches a maximum step limit, which varies according to the scale of the scene. We conduct five trials at each starting location. To accommodate these larger and more varied experiment setups, we also introduce an evaluation metric that is comparable between environments of varying size and complexity:

	Method	824	827	876	880	804	807	812	834	854	879	Mean
Vox@25	○ Classic [8]	17.1±3.7	24.7±7.1	16.9±6.1	14.5±3.4	21.6±0.0	7.6±0.0	18.7±3.7	23.7±7.6	19.5±3.1	20.3±7.0	18.5
	○ NBVP [11]	23.4±3.6	21.6±4.1	23.3±4.4	18.9±1.8	24.5±3.5	17.5±3.3	27.2±3.0	23.4±6.5	26.9±3.2	22.5±5.1	22.9
	○ SEER [15]	23.3±7.4	27.0±4.0	20.4±6.4	24.9±12.0	23.9±7.2	×	25.0±6.2	17.0±9.5	34.7±1.6	25.0±0.8	24.6
	○ Ours	32.2±3.7	33.4±5.5	33.5±4.1	41.3±7.3	26.5±4.1	30.0±2.6	38.3±7.5	30.6±3.0	28.6±2.4	32.2±5.0	32.7
	● Ours	31.3±4.7	34.2±3.3	31.6±4.2	43.5±6.8	29.0±4.7	32.1±2.9	37.0±9.5	29.7±2.8	27.9±4.4	30.7±5.8	32.7
Vox@50	○ Classic	29.1±4.8	37.6±8.0	31.9±7.2	26.1±7.2	39.4±0.0	24.2±0.0	27.7±6.7	37.5±5.6	43.1±4.4	39.2±5.6	33.6
	○ NBVP	46.2±5.7	46.1±5.9	44.5±5.1	31.0±1.3	46.6±4.6	35.3±2.7	49.4±6.6	44.1±3.0	52.3±2.6	45.5±4.8	44.1
	○ SEER	42.1±5.7	42.7±6.3	36.5±11.4	49.5±5.5	35.6±9.3	×	47.3±4.1	24.4±16.8	46.1±4.0	43.6±4.1	40.9
	○ Ours	58.0±4.8	61.9±3.9	58.2±4.2	61.9±7.5	53.9±4.2	64.5±4.6	60.3±8.1	53.7±5.0	72.1±9.8	55.5±5.7	60.0
	● Ours	56.6±7.2	60.1±6.2	51.0±8.6	60.9±4.9	54.6±3.4	45.4±4.4	60.7±7.6	55.3±5.4	53.5±6.6	57.1±3.2	55.5
Vox@100	○ Classic	47.6±1.6	61.2±8.6	45.0±8.2	61.3±5.2	53.7±0.0	45.2±0.0	68.6±10.9	48.3±5.0	54.1±3.7	50.5±5.4	53.6
	○ NBVP	65.0±5.6	78.5±4.9	60.8±9.3	49.8±1.6	69.7±4.8	49.9±2.1	83.4±3.5	70.0±8.8	80.1±20.3	62.6±5.6	67.0
	○ SEER	55.6±5.1	50.7±5.0	51.0±8.6	54.0±3.8	56.6±4.1	×	54.8±7.7	44.2±3.0	48.9±6.8	50.3±2.5	51.8
	○ Ours	71.2±6.0	72.6±8.9	72.0±8.5	68.4±10.8	62.2±8.9	59.8±6.1	82.2±10.1	70.3±10.1	98.3±13.2	58.8±6.5	71.5
	● Ours	73.0±8.5	73.9±6.6	72.7±9.0	70.9±9.3	59.5±6.0	57.7±6.8	80.1±9.0	69.9±11.4	85.1±18.5	62.1±5.2	70.6
Suc.	○ Classic	33.3	86.7	38.0	40.0	6.3	5.6	37.5	31.3	90.0	20.0	38.9
	○ NBVP	100.0	100.0	90.0	50.0	100.0	65.0	100.0	100.0	60.0	100.0	86.5
	○ SEER	60.0	50.0	31.0	50.0	20.0	0.0	80.0	13.3	80.0	20.0	40.4
	○ Ours	100.0	81.3	83.3	100.0	80.0	80.0	100.0	86.7	100.0	75.0	88.6
	● Ours	100.0	68.8	80.0	90.0	80.0	75.0	100.0	90.9	100.0	80.0	86.5

TABLE I: Comparison of mapping efficiency (Vox@k%) and success rate (Suc.) against baseline methods. Methods marked with an unfilled dot ○ use ground-truth depth from the simulator, with a filled dot ● use metric monocular depth estimation [33]. The 3-digit numbers in the first row are scene IDs.

Vox@k(%), the percentage of explored volume relative to the total scene volume when the number of steps reaches $k\%$ of the total steps. A new step is registered when the robot undergoes a significant change in position (> 0.1 m) or orientation ($> 10^\circ$), ensuring both travel distance and rotational coverage are captured. To evaluate exploration efficiency across stages, we set $k = 25, 50, 100$. To determine the statistical steps for $k = 25$ and 50, we calculate the average step count across all methods at which 25% and 50% volume coverage is reached. For $k = 100$, the step count corresponds to the maximum threshold during exploration. This average step threshold is applied to each method individually, measuring the volume coverage achieved at this common step count. This approach ensures interpretability by reflecting the expected performance at a consistent stage across methods, without favoring any specific approach. An exploration round is deemed successful if it achieves $\text{Vox@100} > 40\%$. From this, we compute the average success rate, **Suc.(%)**, for each method across all runs per scene.

B. Result

We conduct experiments to investigate several questions:

How does our system compare to baseline approaches in performance?

Table I summarizes the quantitative results of our experiments. Across all 10 scenes, our method with simulator depth input consistently achieves the highest overall efficiency at 25%, 50%, and 100% of total steps, as well as the highest success rate. Our method using a monocular depth prior ranks second in these metrics, performing better than baseline methods with simulator depth. Notably, at Vox@25, our method outperforms baseline approaches in nine scenes, and at Vox@50, it surpasses all baselines in all 10 scenes, exceeding the second-best method by 16% overall. This demonstrates the ability of our system to effectively prioritize regions with higher info gain early during exploration. It is important to note that all baseline methods rely on simulator depth to ensure accurate 3D maps for extracting candidate exploration poses.

	RGB-only	Depth-only	RGB+Depth
Distance Field Err. (pixels) ↓	0.315	0.167	0.152
Info Gain Cls. Dice Score ↑	0.406	0.403	0.440

TABLE II: Comparison of FrontierNet models with different inputs. Estimated depth is used in this experiment.

Switching to monocular depth estimation would significantly degrade their performance, as inaccurate maps—caused by depth scale errors or artifacts—lead to failures in generating feasible goal poses. In contrast, our method maintains robust performance even with monocular depth inputs. Figure 8 provides qualitative examples of this experiment.

How do the RGB and depth images individually contribute to the performance of FrontierNet?

To explore this, we train multiple FrontierNet models with different input configurations: RGB-only, depth-only, and RGB + depth. We then compare the model performance on a validation set. As shown in II, results indicate that both color and depth information are essential for accurate frontier detection and info gain estimation. Specifically, detection relies predominantly on geometric cues from depth, whereas info gain estimation benefits from both appearance cues from RGB and geometric cues from depth as we have hypothesized.

How much does the distance field and info gain map contribute to the final exploration efficiency?

To address this, we select two scenes and perform exploration with different planner configurations: (1) *df+gain*: using the predicted distance field and info gain; (2) *df+uni*: using the predicted distance field with uniform info gain, assigning the same value to all pixels; (3) *discon+gain*: using the depth discontinuity mask along with info gain. This mask, identical to \mathbf{F}_d in Fig. 4, is extracted from the input depth; and (4) *discon+uni*: using the discontinuity mask with uniform info gain. We track the percentage of mapped volume achieved by each configuration.

As shown in Fig. 9, efficiency and success rate drop when the planner lacks either accurate frontier pixels or info gain. Without info gain, the planner treats all frontiers equally, leading to suboptimal paths prioritizing nearby frontiers. Without

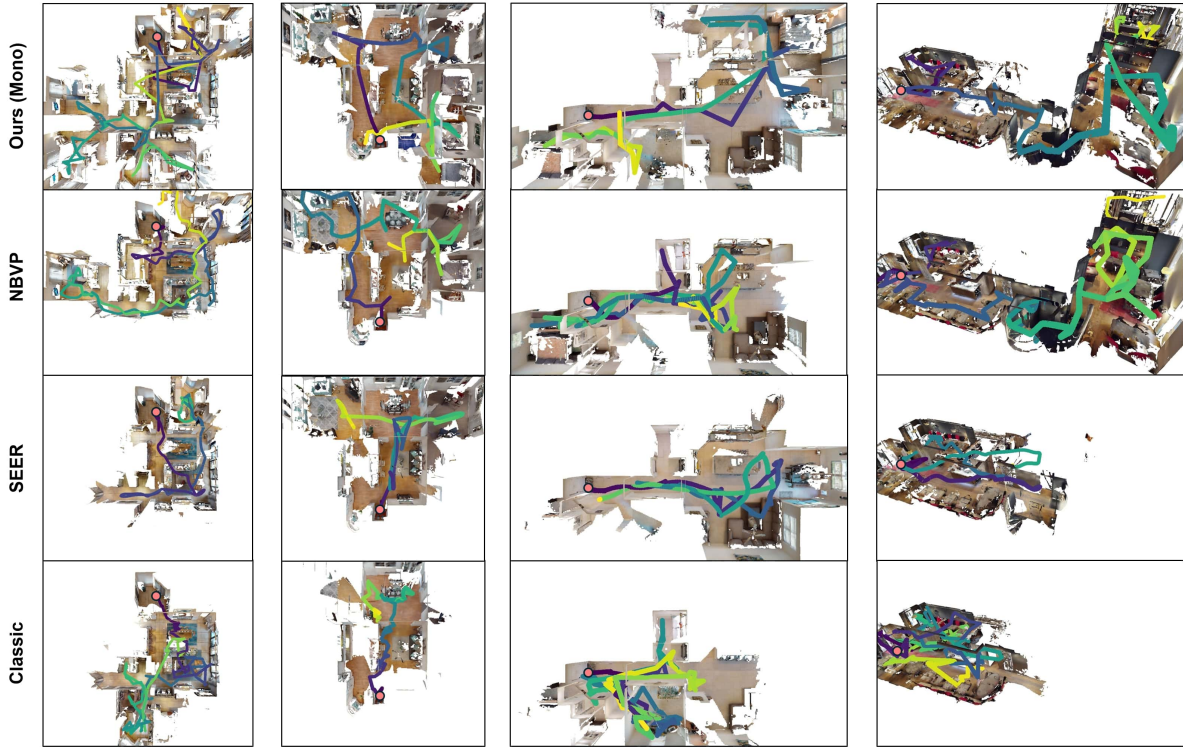


Fig. 8: **Qualitative Comparison:** Exploration path examples of our method compared to three baseline methods across four different scenes (left to right: 876, 824, 880, 854). Starting location is marked as red point. Notably, our approach successfully handles multi-floor environments (scene 854), a challenge for traditional frontier-based methods.

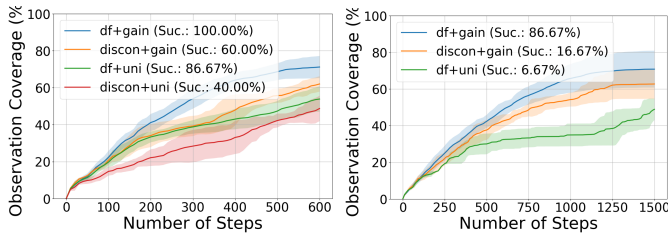


Fig. 9: Performance comparison of different configurations on scene 824 (left) and scene 876 (right). The discon+uni configuration completely fails on scene 876 (0.0% Suc.).

distance field detection, the discontinuity mask generates a noisy, redundant map boundary, adding significant overhead to the process. These results show that both the distance field and info gain map are essential for efficient exploration.

How does our system perform in a fully map-free setup?

As introduced, FrontierNet detects frontiers without requiring a 3D map, and both the frontier update and planning modules can optionally operate without maintaining one. Instead, they solely rely on the frontier detection tree and past robot trajectory. We validated the map-free setup on scene 876. As shown in Fig. 10, with simulator depth, it achieves 23.4 ± 2.0 for Vox@25, 41.9 ± 1.7 for Vox@50, and 55.8 ± 6.0 for Vox@100. Using depth estimation, it achieves 23.9 ± 4.6 , 38.5 ± 3.1 , and 57.2 ± 5.1 , respectively. These results highlight the potential of our system to operate in a fully map-free setup and extend to tasks like object or task-goal navigation.

C. Real-world Validation

We implement our exploration planner as a ROS package and deploy it on a Boston Dynamics Spot robot. A calibrated RGB camera in the front provides 640×480 color images at 3 Hz. The mapping and exploration stacks run on a laptop with

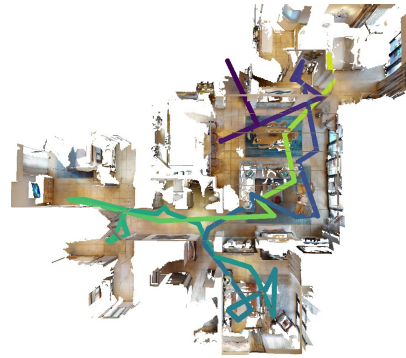


Fig. 10: Exploration result example of our proposed system without building a 3D map. The 3D meshes are used here only for visualization purposes.

an Intel i9-12900HX, 32 GB RAM, and a 16 GB 3080Ti GPU. FrontierNet achieves approximately 5 Hz inference, enabling real-time image processing.

The testing in an indoor environment, see Fig. 11, shows the exploration process. Despite being trained solely on renderings, FrontierNet demonstrates strong robustness to the sim-to-real gap. The robot successfully maps cluttered areas along the main path and progresses toward the opposite side of the entrance without human intervention.

V. CONCLUSION

In this work, we investigate how to leverage both appearance and geometric information from images to enable autonomous exploration. We propose FrontierNet, a hybrid model for 2D frontier detection and info gain prediction, and design an exploration system to integrate seamlessly with FrontierNet. Our system demonstrates significant advantages in exploration efficiency without relying on a 3D map to generate exploration



Fig. 11: Exploration process of a quadrupedal robot in a real-world environment. The mapping result is generated through TSDF integration using monocular depth prediction from the onboard RGB camera.

goals. Its effectiveness is validated through extensive simulation and real-world experiments.

REFERENCES

- [1] M. F. Ginting, D. D. Fan, S.-K. Kim, M. J. Kochenderfer, and A. Agha-mohammadi, "Semantic belief behavior graph: Enabling autonomous robot inspection in unknown environments," *arXiv preprint arXiv:2401.17191*, 2024.
- [2] D. Liu, G. Dissanayake, J. Valls Miro, and K. Waldron, "Infrastructure robotics: Research challenges and opportunities," in *ISARC*, 2014.
- [3] V. A. Ziparo, M. Zaratti, G. Grisetti, T. M. Bonanni, J. Serafin, M. Di Cicco, M. Proesmans, L. Van Gool, O. Vysotska, I. Bogoslavskyi *et al.*, "Exploration and mapping of catacombs with mobile robots," in *SSRR*, 2013.
- [4] J. Chen, B. Sun, M. Pollefeys, and H. Blum, "A 3d mixed reality interface for human-robot teaming," in *ICRA*, 2024.
- [5] C. Gao, F. Daxinger, L. Roth, F. Maffra, P. Beardsley, M. Chli, and L. Teixeira, "Aerial image-based inter-day registration for precision agriculture," in *ICRA*, 2024.
- [6] L. Lobefaro, M. V. Malladi, O. Vysotska, T. Guadagnino, and C. Stachniss, "Estimating 4d data associations towards spatial-temporal mapping of growing plants for agricultural robots," in *IROS*, 2023.
- [7] D. Batra, A. Gokaslan, A. Kembhavi, O. Maksymets, R. Mottaghi, M. Savva, A. Toshev, and E. Wijnmans, "Objectnav revisited: On evaluation of embodied agents navigating to objects," *arXiv preprint arXiv:2006.13171*, 2020.
- [8] B. Yamauchi, "A frontier-based approach for autonomous exploration," in *International Symposium on Computational Intelligence in Robotics and Automation CIRA*, 1997.
- [9] A. Bircher, M. Kamel, K. Alexis, H. Oleynikova, and R. Siegwart, "Receding horizon" next-best-view" planner for 3d exploration," in *ICRA*, 2016.
- [10] N. Yokoyama, S. Ha, D. Batra, J. Wang, and B. Bucher, "Vlfn: Vision-language frontier maps for zero-shot semantic navigation," in *ICRA*, 2024.
- [11] L. Schmid, M. Pantic, R. Khanna, L. Ott, R. Siegwart, and J. Nieto, "An efficient sampling-based method for online informative path planning in unknown environments," *IEEE Robotics and Automation Letters*, 2020.
- [12] A. Dai, S. Papatheodorou, N. Funk, D. Tzoumanikas, and S. Leutenegger, "Fast frontier-based information-driven autonomous exploration with an mav," in *ICRA*, 2020.
- [13] S. Papatheodorou, N. Funk, D. Tzoumanikas, C. Choi, B. Xu, and S. Leutenegger, "Finding things in the unknown: Semantic object-centric exploration with an mav," in *ICRA*, 2023.
- [14] B. Zhou, Y. Zhang, X. Chen, and S. Shen, "Fuel: Fast uav exploration using incremental frontier structure and hierarchical planning," *IEEE Robotics and Automation Letters*, vol. 6, no. 2, pp. 779–786, 2021.
- [15] Y. Tao, Y. Wu, B. Li, F. Cladera, A. Zhou, D. Thakur, and V. Kumar, "Seer: Safe efficient exploration for aerial robots using learning to predict information gain," in *ICRA*, 2023.
- [16] D. S. Chaplot, E. Parisotto, and R. Salakhutdinov, "Active Neural Localization," *ICLR*, 2018.
- [17] C. Cao, H. Zhu, H. Choset, and J. Zhang, "Tare: A hierarchical framework for efficiently exploring complex 3d environments," in *Robotics: Science and Systems*, vol. 5, 2021, p. 2.
- [18] S. Papatheodorou, S. Boche, S. B. Laina, and S. Leutenegger, "Efficient submap-based autonomous mav exploration using visual-inertial slam configurable for lidars or depth cameras," *arXiv preprint arXiv:2409.16972*, 2024.
- [19] W. Gao, M. Booker, A. Adiwahono, M. Yuan, J. Wang, and Y. W. Yun, "An improved frontier-based approach for autonomous exploration," in *2018 15th international conference on control, automation, robotics and vision (ICARCV)*. IEEE, 2018, pp. 292–297.
- [20] M. Selin, M. Tiger, D. Duberg, F. Heintz, and P. Jensfelt, "Efficient autonomous exploration planning of large-scale 3-d environments," *Robotics and Automation Letters*, 2019.
- [21] A. Bircher, M. Kamel, K. Alexis, H. Oleynikova, and R. Siegwart, "Receding horizon path planning for 3d exploration and surface inspection," *Autonomous Robots*, vol. 42, pp. 291–306, 2018.
- [22] L. Schmid, M. N. Cheema, V. Reijgwart, R. Siegwart, F. Tombari, and C. Cadena, "Sc-explorer: Incremental 3d scene completion for safe and efficient exploration mapping and planning," *arXiv preprint arXiv:2208.08307*, 2022.
- [23] Z. Yan, H. Yang, and H. Zha, "Active neural mapping," in *ICCV*, 2023.
- [24] S. Lee, C. Le, W. Jiahao, A. Liniger, S. Kumar, and F. Yu, "Uncertainty guided policy for active robotic 3d reconstruction using neural radiance fields," *IEEE Robotics and Automation Letters*, 2022.
- [25] W. Jiang, B. Lei, and K. Daniilidis, "Fisherrf: Active view selection and uncertainty quantification for radiance fields using fisher information," *arXiv*, 2023.
- [26] W. Jiang, B. Lei, K. Ashton, and K. Daniilidis, "Ag-slam: Active gaussian splatting slam," *arXiv preprint arXiv:2410.17422*, 2024.
- [27] Y. Tao, D. Ong, V. Murali, I. Spasojevic, P. Chaudhari, and V. Kumar, "Rt-guide: Real-time gaussian splatting for information-driven exploration," *arXiv preprint arXiv:2409.18122*, 2024.
- [28] A. Asgharivaskasi and N. Atanasov, "Active bayesian multi-class mapping from range and semantic segmentation observations," in *ICRA*, 2021.
- [29] Y. Tao, X. Liu, I. Spasojevic, S. Agarwal, and V. Kumar, "3d active metric-semantic slam," *IEEE Robotics and Automation Letters*, 2024.
- [30] D. S. Chaplot, M. Dalal, S. Gupta, J. Malik, and R. R. Salakhutdinov, "Seal: Self-supervised embodied active learning using exploration and 3d consistency," *NeurIPS*, 2021.
- [31] J. Chen, G. Li, S. Kumar, B. Ghanem, and F. Yu, "How to not train your dragon: Training-free embodied object goal navigation with semantic frontiers," *arXiv preprint arXiv:2305.16925*, 2023.
- [32] K. Qu, J. Tan, T. Zhang, F. Xia, C. Cadena, and M. Hutter, "Ippon: Common sense guided informative path planning for object goal navigation," *arXiv preprint arXiv:2410.19697*, 2024.
- [33] M. Hu, W. Yin, C. Zhang, Z. Cai, X. Long, H. Chen, K. Wang, G. Yu, C. Shen, and S. Shen, "Metric3d v2: A versatile monocular geometric foundation model for zero-shot metric depth and surface normal estimation," *arXiv preprint arXiv:2404.15506*, 2024.
- [34] R. Pautrat, D. Barath, V. Larsson, M. R. Oswald, and M. Pollefeys, "Deepsls: Line segment detection and refinement with deep image gradients," in *CVPR*, 2023.
- [35] N. Xue, T. Wu, S. Bai, F. Wang, G.-S. Xia, L. Zhang, and P. H. Torr, "Holistically-attracted wireframe parsing," in *CVPR*, 2020.
- [36] S. F. Bhat, I. Alhashim, and P. Wonka, "Adabins: Depth estimation using adaptive bins," in *Proceedings of the IEEE/CVF conference on computer vision and pattern recognition*, 2021, pp. 4009–4018.
- [37] S. K. Ramakrishnan, A. Gokaslan, E. Wijnmans, O. Maksymets, A. Clegg, J. Turner, E. Undersander, W. Galuba, A. Westbury, A. X. Chang *et al.*, "Habitat-matterport 3d dataset (hm3d): 1000 large-scale 3d environments for embodied ai," *arXiv:2109.08238*, 2021.
- [38] K. He, X. Zhang, S. Ren, and J. Sun, "Deep residual learning for image recognition," in *CVPR*, 2016.
- [39] O. Russakovsky, J. Deng, H. Su, J. Krause, S. Satheesh, S. Ma, Z. Huang, A. Karpathy, A. Khosla, M. Bernstein *et al.*, "Imagenet large scale visual recognition challenge," *IJCV*, 2015.
- [40] L. Schmid, V. Reijgwart, L. Ott, J. Nieto, R. Siegwart, and C. Cadena, "A unified approach for autonomous volumetric exploration of large scale environments under severe odometry drift," *IEEE Robotics and Automation Letters*, vol. 6, no. 3, pp. 4504–4511, 2021.
- [41] R. J. Campello, D. Moulavi, and J. Sander, "Density-based clustering based on hierarchical density estimates," in *Pacific-Asia conference on knowledge discovery and data mining*. Springer, 2013, pp. 160–172.
- [42] Q.-Y. Zhou, J. Park, and V. Koltun, "Open3d: A modern library for 3d data processing," *arXiv preprint arXiv:1801.09847*, 2018.
- [43] A. Hornung, K. M. Wurm, M. Bennewitz, C. Stachniss, and W. Burgard, "OctoMap: An efficient probabilistic 3D mapping framework based on octrees," *Autonomous Robots*, 2013.
- [44] I. A. Şucan, M. Moll, and L. E. Kavraki, "The Open Motion Planning Library," *IEEE Robotics & Automation Magazine*, 2012.